LETTER

doi:10.1038/nature13455

Giant nonlinear response from plasmonic metasurfaces coupled to intersubband transitions

Jongwon Lee[1], Mykhailo Tymchenko[1], Christos Argyropoulos[1], Pai-Yen Chen[1], Feng Lu[1], Frederic Demmerle[2], Gerhard Boehm[2], Markus-Christian Amann[2], Andrea Alù[1] & Mikhail A. Belkin[1]

Intersubband transitions in n-doped multi-quantum-well semiconductor heterostructures make it possible to engineer one of the largest known nonlinear optical responses in condensed matter systems—but this nonlinear response is limited to light with electric field polarized normal to the semiconductor layers[1–7]. In a different context, plasmonic metasurfaces (thin conductor–dielectric composite materials) have been proposed as a way of strongly enhancing light–matter interaction and realizing ultrathin planarized devices with exotic wave properties[8–11]. Here we propose and experimentally realize metasurfaces with a record-high nonlinear response based on the coupling of electromagnetic modes in plasmonic metasurfaces with quantum-engineered electronic intersubband transitions in semiconductor heterostructures. We show that it is possible to engineer almost any element of the nonlinear susceptibility tensor of these structures, and we experimentally verify this concept by realizing a 400-nm-thick metasurface with nonlinear susceptibility of greater than 5×10^4 picometres per volt for second harmonic generation at a wavelength of about 8 micrometres under normal incidence. This susceptibility is many orders of magnitude larger than any second-order nonlinear response in optical metasurfaces measured so far[12–15]. The proposed structures can act as ultrathin highly nonlinear optical elements that enable efficient frequency mixing with relaxed phase-matching conditions, ideal for realizing broadband frequency up- and down-conversions, phase conjugation and all-optical control and tunability over a surface.

Many demonstrated applications of optical metamaterials are based on their linear interaction with light, including super-resolution imaging[16,17] and optical cloaking[18–20]. More recently, optical metamaterials with tailored nonlinear response have provided new degrees of freedom in metamaterial design, with interesting uses in super-resolution imaging[21], performing efficient frequency conversion and optical control with greatly relaxed phase-matching conditions[22], and in optical switching and memories at the nanoscale[23].

So far, nonlinearities in metamaterials have been mostly realized by exploiting the natural nonlinear response of plasmonic metals[12,13] or by enhancing the nonlinearity of optical crystals using plasmonic nanoantennas[14,15]. A different approach to realizing large nonlinear optical response has been put forward—quantum-engineering electronic intersubband transitions in n-doped multi-quantum-well (MQW) semiconductor heterostructures[1–7]. By controlling the widths of wells and barriers in the MQW structures, one can tailor the transition energy and dipole moments between electron subbands so as to maximize the quantum-mechanical expression for a nonlinear process of choice; this process can produce one of the largest known nonlinear responses, up to six orders of magnitude larger than that of traditional nonlinear optical materials[1–7]. Voltage may be used to modify and spectrally tune intersubband nonlinearities[3], and electrical pumping may be used to produce active intersubband structures with full loss-compensation for both second-order[5–7] and third-order[24] nonlinear processes.

Nonlinear MQW structures have been successfully integrated into waveguide-based systems so as to produce efficient frequency conversion[2,4–7,25], and have enabled the development of mass-producible room-temperature electrically pumped sources of THz radiation[7]. A power conversion efficiency of nearly 1% for second harmonic generation (SHG) at a 8.6 μm fundamental frequency was achieved in waveguides with passive $\mathrm{In_{0.53}Ga_{0.47}As/Al_{0.48}In_{0.52}As}$ MQW structures[25] and a power conversion efficiency of over 16% was theoretically predicted[26]. However, the integration of giant MQW nonlinearities with free-space optics is very challenging, because optical transitions between electron subbands are intrinsically polarized along the surface normal to the MQW layers (taken to be the z axis in this Letter).

In a different context, properly patterned metallic surfaces supporting highly confined plasmonic resonances have been proposed for a variety of applications, including enhanced light–matter interaction at the subwavelength scale, polarization conversion, control of optical transmission and radiation, enhanced chirality, asymmetric transmission and filtering[11]. In order to overcome the present limitations of MQW systems, and further enhance the intersubband nonlinear response, we propose combining the MQW layered substrates with suitably designed plasmonic metasurfaces. In the following we theoretically and experimentally demonstrate that, by combining quantum-electronic engineering of intersubband nonlinearities with electromagnetic engineering of plasmonic nanoresonators, we can produce ultrathin, planarized, highly nonlinear optical metasurfaces. This approach allows us to create large-area metasurfaces in which virtually any element of the nonlinear susceptibility tensor may be *ad hoc* engineered to have a giant nonlinear response. The impact of these ultrathin devices may be substantial in a variety of fields, including THz generation and detection, phase conjugation, and other nonlinear processes.

Figure 1a shows the band diagram of a coupled quantum well structure, repeated multiple times to produce the 400-nm-thick MQW layer used in our experiments. This structure is designed to support a giant resonant nonlinear response for SHG at $1/\lambda \approx 1{,}240\ \mathrm{cm}^{-1}$ ($\lambda \approx 8\ \mu\mathrm{m}$). Figure 1b plots the absolute value of the SHG nonlinear susceptibility tensor element $\chi^{(2)}_{zzz}$ as a function of pump frequency calculated for this structure as described in Methods. The nonlinear response peaks at approximately $54\ \mathrm{nm\ V}^{-1}$, nearly 3 orders of magnitude larger than the largest $\chi^{(2)}$ coefficient of natural optical materials[27].

The MQW layer is then sandwiched between a metal ground plane and a patterned array of metallic nanostructures (Fig. 1c, d). This grounded metasurface can be designed to enable efficient coupling of plasmonic modes with z-polarized intersubband transitions, drastically enhancing light–matter interaction and converting the impinging transverse field polarization to the desired z-direction[28]. Even though a ground plane is used in our metasurface design, efficient coupling of intersubband transitions with resonant metallic nanostructures may also be achieved without using a ground plane, as shown recently[29], which may allow the results presented here to be translated into transmission mode.

Since our goal is to enhance SHG, the plasmonic nanostructures are designed to induce and enhance the local electric field at both fundamental frequency (FF) ω and the second-harmonic frequency (SH) 2ω. The plasmonic nanostructures must also lack inversion symmetry

---

[1]Department of Electrical and Computer Engineering, The University of Texas at Austin, Austin, Texas 78712, USA. [2]Walter Schottky Institut, Technische Universität München, Am Coulombwall 4, Garching 85748, Germany.

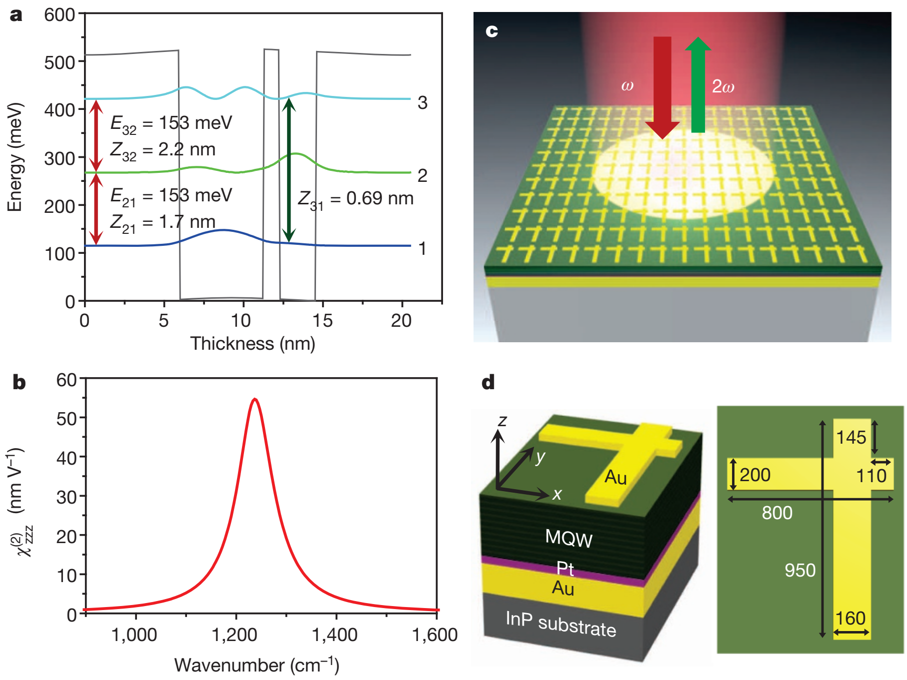

Figure 1 | Nonlinear metasurface structure. **a**, Conduction band diagram of one period of an $In_{0.53}Ga_{0.47}As/Al_{0.48}In_{0.52}As$ coupled quantum well structure designed for giant nonlinear response for SHG. The moduli squared of the electron wavefunctions for subbands 1, 2 and 3 are shown and labelled accordingly. Transitions between pairs of electron subbands are marked with double-headed red arrows, and the values of the transition energies (E_{21} and E_{32}) and dipole moments (Z_{21}, Z_{32} and Z_{31}) are shown next to each arrow. **b**, Intersubband nonlinear susceptibility of the structure in **a** as a function of pump frequency for SHG. **c**, Schematic of the metasurface design and operation. Red and green arrows indicate the incident pump beam at fundamental frequency ω and the reflected second-harmonic beam at frequency 2ω, respectively. **d**, A 1,000 nm × 1,300 nm metasurface unit cell (left), dimensions of the nanocross are given in nm (right).

in the *x*–*y* plane, otherwise all nonlinear susceptibility tensor elements $\chi^{(2)}_{ijk}$ with *i*, *j* and *k* being *x* or *y* would vanish by symmetry.

Our starting design strategy consists of an array of 'L'-shaped nanostructures, whose two arms have been shown in recent papers to support two independently tunable plasmonic resonances that can be used for polarization control[30,31]. After several rounds of optimization, we converged on the nanostructure shown in Fig. 1d, consisting of an asymmetric nanocross with the two orthogonal arms connected in such a way as to ensure good modal overlap between the resonances at ω and 2ω, yet possessing a strong asymmetry to support large $\chi^{(2)}_{ijk}$. The dimensions of the nanocross optimized for SHG at $1/\lambda = 1{,}240\ \mathrm{cm}^{-1}$ are shown in Fig. 1d and the results of our full-wave electromagnetic simulations are shown in Fig. 2. In particular, Fig. 2a–h shows the normalized E_z field component induced in the MQW layer for different FF and SH input light polarizations at normal incidence. The computed fields are normalized to the input (transverse) field amplitude impinging at normal incidence. Significant E_z field is induced in the MQW at both ω and 2ω, up to five times the amplitude of the transverse impinging field.

The effective second-order nonlinear susceptibility tensor of the metasurface ($\overleftrightarrow{\chi}^{(2)\mathrm{eff}}$) may be related to these field distributions by using the Lorentz reciprocity theorem[32], as described in the Methods section, yielding the expression for the general *ijk* element

$$\chi^{(2)\mathrm{eff}}_{ijk} = \chi^{(2)}_{zzz} \frac{\int_V E^{2\omega}_{z(i)}(x,y,z)E^{\omega}_{z(j)}(x,y,z)E^{\omega}_{z(k)}(x,y,z)\mathrm{d}V}{E^{2\omega}_{i(\mathrm{inc})}E^{\omega}_{j(\mathrm{inc})}E^{\omega}_{k(\mathrm{inc})}V} \qquad (1)$$

where $E^{\omega}_{z(i)}$ and $E^{2\omega}_{z(i)}$ are the local E_z field components in the MQW layer induced by *i*-polarized incident waves $E^{\omega}_{i(\mathrm{inc})}$ and $E^{2\omega}_{i(\mathrm{inc})}$, respectively, at frequencies ω and 2ω, respectively, *i* can be *x*, *y* or *z*, and the integration covers the volume (*V*) of the MQW layer in the unit cell.

Equation (1) shows that we can engineer essentially any component of the nonlinear susceptibility tensor of the metasurface and further increase the already giant nonlinear response from intersubband transitions using local field enhancement at ω and 2ω. It also confirms the necessity of inducing a strong modal overlap between the fundamental and SH modes in the nanostructures, for which our metasurface is optimized. This result may be readily generalized to other nonlinear processes of interest. Using equation (1) and simulated field distributions for the nanocross structure in Fig. 2, we calculate that the largest nonlinear susceptibility coefficient for normal light incidence at an input wavenumber of $1{,}240\ \mathrm{cm}^{-1}$ is $\chi^{(2)\mathrm{eff}}_{yyy} = 31\ \mathrm{nm\ V}^{-1}$, followed by $\chi^{(2)\mathrm{eff}}_{xxx} = 25\ \mathrm{nm\ V}^{-1}$, $\chi^{(2)\mathrm{eff}}_{xyy} = 6.5\ \mathrm{nm\ V}^{-1}$ and $\chi^{(2)\mathrm{eff}}_{yxx} = 3.9\ \mathrm{nm\ V}^{-1}$.

Figure 2i shows the computed linear absorption spectrum of the metasurface. The calculated SH power versus FF pump power for different input/output polarization combinations is shown in Fig. 2j. Results are given for *yyy*, *xxx*, *xyy* and *yxx* polarization combinations, where the first index refers to the polarization of the SH beam, and the last two indices refer to the polarization of the FF beam.

For experimental testing, a 400-nm-thick MQW layer was transferred onto a metal ground plane and a 400 μm × 400 μm two-dimensional array of nanocrosses was fabricated on top of the MQW layer to produce the structure shown in Fig. 1c. Fabrication details are provided in Methods. To accommodate the uncertainty in material parameters and fabrication errors, we fabricated several arrays with nanocross dimensions slightly varying around the optimal theoretical parameters shown in Fig. 1d. The description below focuses on the measured array with highest SHG generation efficiency at $1{,}240\ \mathrm{cm}^{-1}$, but we stress that the measured nonlinear response is quite robust to small changes in the design parameters, as several of our realized metasurface samples showed a similarly large nonlinear response. Yet we verified that metasurfaces with plasmonic resonances significantly detuned from the intersubband transition frequencies of the MQW structure produced, as expected, little or no nonlinear response (see Methods for details). This confirms the unique property of the proposed metasurface, combining quantum and electromagnetic engineering of its nonlinear response.

Figure 3 shows a scanning electron microscope (SEM) image of the nanocross array (Fig. 3a) and a side view of the cleaved facet with the MQW layer metal-bonded to the InP substrate (Fig. 3b). The absorption spectra of the metasurface for *x*- and *y*-polarized input light at normal incidence are shown in Fig. 3c. The experimental shapes and positions of the peaks are in reasonable agreement with the simulated spectrum in Fig. 2i.

SHG measurements of the metasurface were performed using the setup shown in Fig. 3d and described in the figure legend. SHG peak power as a function of the square of the FF peak power and the square of the FF peak intensity is plotted in Fig. 4a for different input/output polarization combinations. The highest SHG generation efficiency is achieved for the *yyy* polarization combination, followed by *xxx*, *yxx* and *xyy* polarization combinations, in agreement with the theoretical predictions shown in Fig. 2j. Comparably strong nonlinear responses were also observed for the same metasurface for a 45° incidence angle geometry, indicating that

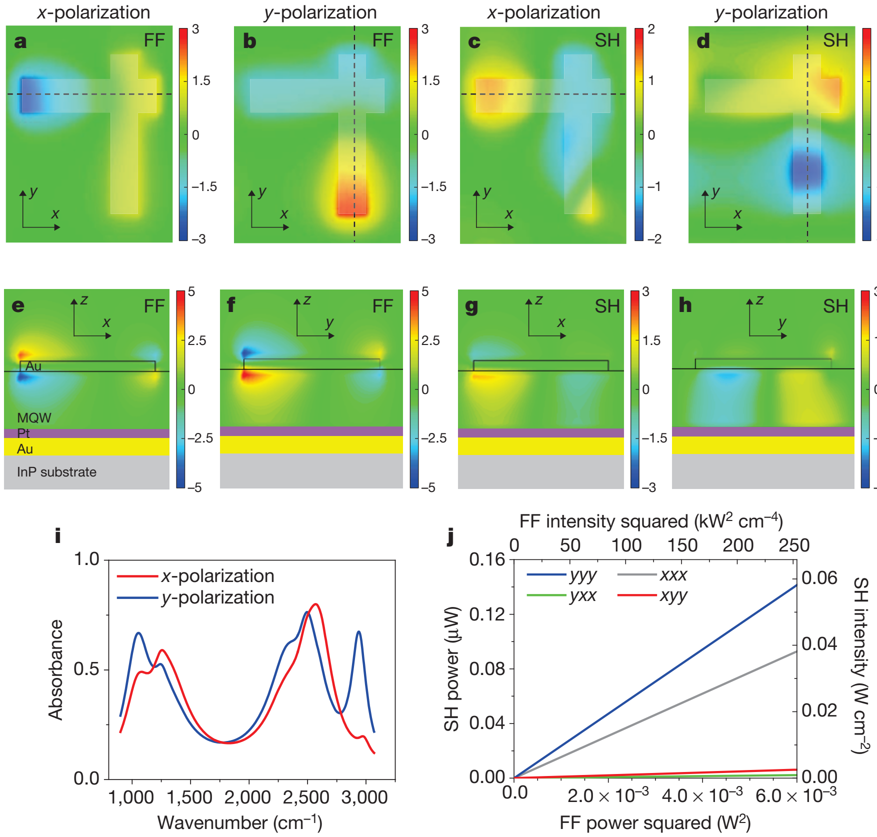

Figure 2 | Simulations and predicted performance of the metasurface geometry. **a**–**d**, Top view cross-section of the calculated E_z field enhancement monitored in the MQW layer 100 nm below the gold plasmonic resonators at FF (**a**, **b**) and SH frequency (**c**, **d**). **e**–**h**, Side view cross-section of the calculated E_z field enhancement monitored along the dashed lines shown in **a**–**d** respectively at FF (**e**, **f**) and SH frequency (**g**, **h**). The data are shown for incident light polarized along the x-axis and the y-axis of the structure. **i**, Computed absorption spectrum of the proposed metasurface for different input light polarization. **j**, SHG power (left axis) and intensity (right axis) versus the square of the FF power (bottom axis) and intensity (top axis) for different input/output polarization combinations at FF wavenumber $1/\lambda = 1{,}240\ \mathrm{cm}^{-1}$. The FF focal spot is assumed to be of a Gaussian shape with a diameter of $2w = 35\ \mu\mathrm{m}$, as in the experiments (Methods).

our structures may be operated without constraints on the incidence and observation angles (see Methods for details).

From equation (1) and the detailed analysis in the Methods section, one expects to observe a linear dependence of SH power on the square of FF power in Fig. 4a. However, as indicated in the figure, the slope of the curve changes: for example, for the *yyy* polarization combination, the slope changes from 57 μW W^{-2} for low FF powers to 23 μW W^{-2} for higher FF powers. We attribute this effect to intensity saturation of intersubband transitions[33] in our MQW structures, and provide further experimental evidence in support of this conclusion in Methods. Calculations shown in Methods indicate that the saturation intensity[33] for the state 1 to state 2 transition (see Fig. 1) in our structures is approximately 0.47 MW cm^{-2}, and simulation results in Fig. 2 indeed indicate local intensities approaching saturation intensity in the hotspots of the MQW structure for input pump intensities above 10 kW cm^{-2}. We note that our proof-of-concept metasurface design is far from perfect, as one ideally wants to create a more uniform local field enhancement within the MQW structure at both FF and SH frequencies with maximal modal overlap integrals, consistent with equation (1). This implies that an even larger nonlinear response may be found with better optimized nanoresonator designs, exploiting the field localization properties of plasmonic structures. Yet the measured results presented here reveal an enormous potential for the proposed metasurface.

To better understand the potential improvement associated with nanoresonator optimization, consider an ideal metasurface in which the nanoresonators are able to induce a uniform E_z field enhanced 3 times compared to the impinging field across the entire MQW layer at both SH and FF. In this case, equation (1) predicts $\chi^{(2)\mathrm{eff}} = 27\chi^{(2)}_{zzz}$, approximately 50 times larger than the largest $\chi^{(2)\mathrm{eff}}$ coefficients computed for the nanocross design used in this work. Since the SHG power scales with $\left|\chi^{(2)\mathrm{eff}}\right|^2$, such a metasurface would produce over three orders of magnitude

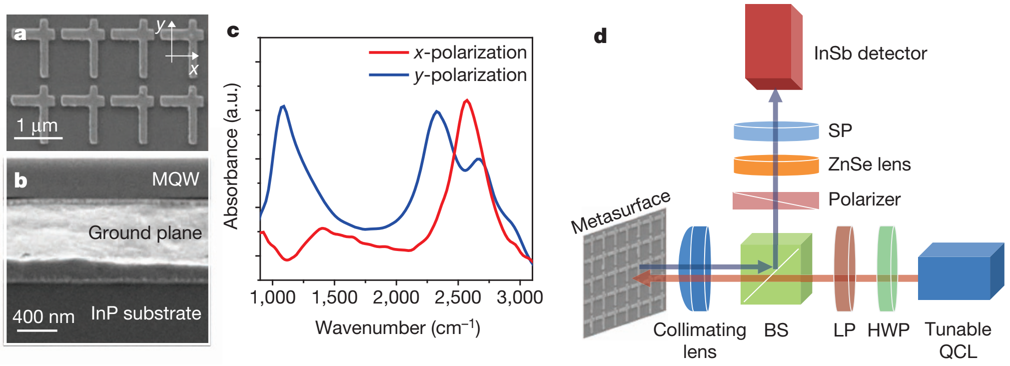

Figure 3 | Characterization of processed metasurface. **a**, **b**, Scanning electron microscope images of the fabricated metasurface, top (**a**) and side (**b**) view. **c**, Absorption spectrum of the fabricated metasurface for normally incident light polarized along x-axis and y-axis of nanocrosses, as shown in **a**. **d**, Optical set-up for metasurface characterization. Linearly polarized light from a tunable quantum cascade laser passes through an achromatic half-wave plate (HWP) for polarization control, a long pass filter (LP) to remove SH light coming from the laser, a non-polarizing achromatic 50/50 beam splitter (BS), and a numerical aperture 0.5 collimating lens to the sample. SHG output is collected by the same lens and is directed by the beam splitter towards the detector through a polarizer, a ZnSe lens, and a short pass filter (SP) that is used to block FF.

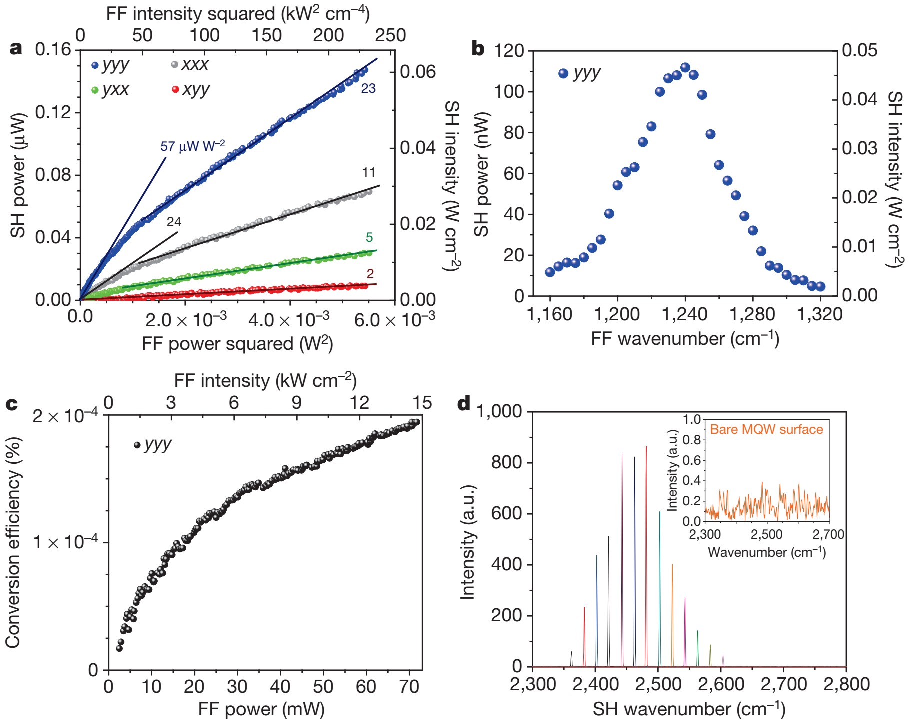

Figure 4 | Nonlinear response from the metasurface. **a**, SH peak power (left axis) and intensity (right axis) output as a function of FF peak power squared (bottom axis) or peak intensity squared (top axis) at an FF wavenumber of 1,240 cm^{-1} for different input/output polarization combinations (see key). Straight lines and labels indicate slopes of SH peak power dependence on FF power squared. **b**, SH peak power (left axis) and peak intensity (right axis) as a function of FF wavenumber for the *yyy* polarization combination. FF peak power was fixed at 30 mW for the measurements. **c**, SHG power conversion efficiency as a function of FF peak power (bottom axis) or peak intensity (top axis) at an FF wavenumber of 1,240 cm^{-1} for the *yyy* polarization combination. **d**, Spectra of SH output for different pump wavenumbers. Inset, no SH emission is observable for a bare MQW surface with no nanostructures on it. Measurements in **a**–**d** are performed at normal FF incidence/normal SH reflection.

improvement in SHG conversion efficiency compared to our current experiment. Furthermore, since the field enhancement is limited to a factor of 3, no significant intensity saturation is expected for the pump intensities used in our experiment. Improvements may also be achieved by exploring the quantum-engineering design space of our structures. The simple doubly-resonant quantum well heterostructure used here for this initial proof-of-concept demonstration is by no means the optimal design, and more sophisticated designs may be devised to achieve both higher nonlinearity and much larger saturation intensity, similar to those described in refs 25 and 26.

Our MQW structure and plasmonic nanocrosses were designed to provide maximum SHG efficiency at a pump wavenumber of $1/\lambda \approx 1{,}240\ \mathrm{cm}^{-1}$. This is experimentally confirmed in Fig. 4b, where we record SHG power output as a function of pump frequency while keeping the pump power constant. The *yyy* SHG power conversion efficiency for an FF wavenumber of 1,240 cm^{-1} is shown in Fig. 4c. We achieve a power conversion efficiency of almost 2×10^{-6} using a pump intensity of only 15 kW cm^{-2}. In comparison, previously demonstrated nonlinear optical metasurfaces at infrared or visible frequencies required high-peak-power fs lasers providing over 10^8 W cm^{-2} FF intensity to produce an SHG power conversion efficiency of 10^{-10} to 10^{-11} (refs 12–15). Assuming identical low pumping intensity, our metasurfaces achieve over 8 orders of magnitude enhancement in conversion efficiency over the current state-of-the-art.

Experimental values of $\chi_{ijk}^{(2)\mathrm{eff}}$ are obtained using the intensity data for SH and FF beams in Fig. 4 as described in Methods. We obtain $\chi_{yyy}^{(2)\mathrm{eff}} \approx 55\ \mathrm{nm\,V^{-1}}$ (35 nm V^{-1}) and $\chi_{xxx}^{(2)\mathrm{eff}} \approx 36\ \mathrm{nm\,V^{-1}}$ (24 nm V^{-1}) for low FF intensity (high FF intensity) in Fig. 4a. The other two coefficients have no significant dependence on pump intensity in the experiment: $\chi_{yxx}^{(2)\mathrm{eff}} \approx 16\ \mathrm{nm\,V^{-1}}$ and $\chi_{xyy}^{(2)\mathrm{eff}} = 10\ \mathrm{nm\,V^{-1}}$. All these quantities are in good agreement with our theoretical predictions, given uncertainties in material parameters and $\chi_{zzz}^{(2)}$. Finally, Fig. 4d shows SHG emission spectra from the metasurface for different FF. The MQW structure without patterned nanostructures does not produce any significant nonlinear response for normal incidence, as shown in the figure inset.

Our proof-of-concept experiment may be extended in a variety of ways: for example, to create voltage-tunable[3] and active electrically pumped nonlinear metasurfaces[5–7], and to spectrally and spatially engineer the nonlinear optical response in more general ways. The metasurfaces with giant nonlinear optical response presented here may serve as the foundation for a flat nonlinear optics paradigm, in which efficient frequency mixing may occur over deeply subwavelength films with significantly relaxed phase-matching conditions (compared to those required for bulk nonlinear crystals) that only require matching of wavevector components parallel to the surface. Such ultrathin nonlinear materials may dramatically simplify wave-mixing experiments in a variety of set-ups, and find application in frequency up- and down-conversion, mixing, phase conjugation, all-optical control and tunability, as well as in photon pair generation over a surface for quantum information processing.

METHODS SUMMARY

The $\mathrm{In_{0.53}Ga_{0.47}As/Al_{0.48}In_{0.52}As}$ coupled quantum well structure for nonlinear response shown in Fig. 1a was designed using a self-consistent Poisson-Schrodinger solver. The layer sequence (in nanometres) is **6.0**/5.3/**1**/2.3/**6.0**, where AlInAs barriers are shown in bold, and the first 3 nm of the first 6-nm barrier and the last 3 nm of the last 6-nm barrier are n-doped to $5 \times 10^{17}\ \mathrm{cm^{-3}}$. A 577-nm-thick MQW layer composed of 28 repetitions of the structure in Fig. 1a was grown by molecular beam epitaxy on a semi-insulating InP substrate. The layer was then transferred to another gold-coated semi-insulating InP substrate via thermo-compression bonding and thinned down to approximately 400 nm thickness by chemical etching. A commercial Maxwell's equations solver based on the finite-integration method was used for the electromagnetic simulations. Experimentally, a 400 μm × 400 μm two-dimensional array of plasmonic nanoresonators was patterned onto the top of the MQW layer via e-beam lithography, metal evaporation, and lift-off. Linear optical characterization of the metasurface was done in reflection mode using a Fourier-transform infrared spectrometer (FTIR) equipped with a liquid-nitrogen-cooled HgCdTe photodetector. Nonlinear optical characterization was done using the optical set-up shown in Fig. 3d. A pulsed broadly-tunable quantum cascade laser was used for pumping and a calibrated InSb detector was used for SHG signal detection. We assume a Gaussian beam shape on the metasurface with an intensity distribution for FF given as $I_{\mathrm{FF}}e^{-2r^2/w^2}$ and that for SH given as $I_{\mathrm{SH}}e^{-4r^2/w^2}$. The FF focal spot diameter was measured by the knife-edge technique to be $2w = 35\ \mu\mathrm{m}$.

Online Content Methods, along with any additional Extended Data display items and Source Data, are available in the online version of the paper; references unique to these sections appear only in the online paper.

Received 27 September 2013; accepted 9 May 2014.

1. Fejer, M. M. *et al.* Observation of extremely large quadratic susceptibility at 9.6–10.8 μm in electric-field-biased AlGaAs quantum wells. *Phys. Rev. Lett.* **62,** 1041–1044 (1989).

2. Rosencher, E., Bois, P., Nagle, J. & Delaitre, S. Second harmonic generation by intersubband transitions in compositionally asymmetrical MQWs. *Electron. Lett.* **25,** 1063–1065 (1989).
3. Capasso, F., Sirtori, C. & Cho, A. Y. Coupled-quantum-well semiconductors with giant electric-field tunable nonlinear-optical properties in the infrared. *IEEE J. Quantum Electron.* **30,** 1313–1326 (1994).
4. Rosencher, E. *et al.* Quantum engineering of optical nonlinearities. *Science* **271,** 168–173 (1996).
5. Gmachl, C. *et al.* Optimized second-harmonic generation in quantum cascade lasers. *IEEE J. Quantum Electron.* **39,** 1345–1355 (2003).
6. Belkin, M. A. *et al.* Terahertz quantum-cascade-laser source based on intracavity difference-frequency generation. *Nature Photon.* **1,** 288–292 (2007).
7. Vijayraghavan, K. *et al.* Broadly tunable terahertz generation in mid-infrared quantum cascade lasers. *Nature Commun.* **4,** 2021 (2013).
8. Liu, X. L. *et al.* Taming the blackbody with infrared metamaterials as selective thermal emitters. *Phys. Rev. Lett.* **107,** 045901 (2011).
9. Yu, N. F. *et al.* Light propagation with phase discontinuities: generalized laws of reflection and refraction. *Science* **334,** 333–337 (2011).
10. Ni, X. J. *et al.* Broadband light bending with plasmonic nanoantennas. *Science* **335,** 427 (2012).
11. Monticone, F., Estakhri, N. M. & Alu, A. Full control of nanoscale optical transmission with a composite metascreen. *Phys. Rev. Lett.* **110,** 203903 (2013).
12. Klein, M. W., Enkrich, C., Wegener, M. & Linden, S. Second-harmonic generation from magnetic metamaterials. *Science* **313,** 502–504 (2006).
13. Feth, N. *et al.* Second-harmonic generation from complementary split-ring resonators. *Opt. Lett.* **33,** 1975–1977 (2008).
14. Fan, W. J. *et al.* Second harmonic generation from patterned GaAs inside a subwavelength metallic hole array. *Opt. Express* **14,** 9570–9575 (2006).
15. Niesler, F. B. P. *et al.* Second-harmonic generation from split-ring resonators on a GaAs substrate. *Opt. Lett.* **34,** 1997–1999 (2009).
16. Pendry, J. B. Negative refraction makes a perfect lens. *Phys. Rev. Lett.* **85,** 3966–3969 (2000).
17. Fang, N., Lee, H., Sun, C. & Zhang, X. Sub-diffraction-limited optical imaging with a silver superlens. *Science* **308,** 534–537 (2005).
18. Leonhardt, U. Optical conformal mapping. *Science* **312,** 1777–1780 (2006).
19. Pendry, J. B., Schurig, D. & Smith, D. R. Controlling electromagnetic fields. *Science* **312,** 1780–1782 (2006).
20. Chen, P. Y., Soric, J. & Alu, A. Invisibility and cloaking based on scattering cancellation. *Adv. Mater.* **24,** Op281–Op304 (2012).
21. Pendry, J. B. Time reversal and negative refraction. *Science* **322,** 71–73 (2008).
22. Rose, A. & Smith, D. R. Overcoming phase mismatch in nonlinear metamaterials. *Opt. Mater. Express* **1,** 1232–1243 (2011).
23. Argyropoulos, C. *et al.* Nonlinear plasmonic cloaks to realize giant all-optical scattering switching. *Phys. Rev. Lett.* **108,** 263905 (2012).
24. Hugi, A. *et al.* Mid-infrared frequency comb based on a quantum cascade laser. *Nature* **492,** 229–233 (2012).
25. Vodopyanov, K. L. *et al.* Phase-matched second harmonic generation in asymmetric double quantum wells. *Appl. Phys. Lett.* **72,** 2654–2656 (1998).
26. Vurgaftman, I., Meyer, J. R. & RamMohan, L. R. Optimized second-harmonic generation in asymmetric double quantum wells. *IEEE J. Quantum Electron.* **32,** 1334–1346 (1996).
27. Boyd, R. W. *Nonlinear Optics* (Academic, 2008).
28. Todorov, Y. *et al.* Ultrastrong light-matter coupling regime with polariton dots. *Phys. Rev. Lett.* **105,** 196402 (2010).
29. Benz, A. *et al.* Strong coupling in the sub-wavelength limit using metamaterial nanocavities. *Nature Commun.* **4,** 2882 (2013).
30. Ellenbogen, T., Seo, K. & Crozier, K. B. Chromatic plasmonic polarizers for active visible color filtering and polarimetry. *Nano Lett.* **12,** 1026–1031 (2012).
31. Zhao, Y. & Alu, A. Tailoring the dispersion of plasmonic nanorods to realize broadband optical meta-waveplates. *Nano Lett.* **13,** 1086–1091 (2013).
32. Balanis, C. A. *Advanced Engineering Electromagnetics* (Wiley, 1989).
33. Vodopyanov, K. L. *et al.* Intersubband absorption saturation study of narrow III–V multiple quantum wells in the $\lambda=2.8$–$9\ \mu$m spectral range. *Semicond. Sci. Technol.* **12,** 708–714 (1997).

Acknowledgements This work was supported by NSF EAGER grant no. 1348049 (to M.A.B. and A.A.), AFOSR YIP award no. FA9550-10-1-0076 (M.A.B.), AFOSR YIP award no. FA9550-11-1-0009 (A.A.), and ONR MURI grant no. N00014-10-1-0942 (A.A.). The Walter Schottky Institute group acknowledges support from the Excellence Cluster 'Nano Initiative Munich (NIM)'. Sample fabrication was carried out in the Microelectronics Research Center at the University of Texas at Austin, which is a member of the National Nanotechnology Infrastructure Network.

Author Contributions J.L. designed the semiconductor heterostructure, calculated physical parameters and performed all fabrication and experimental measurements; M.T., C.A. and P.-Y.C. performed theoretical computations and structure optimization; F.L. assisted in experimental measurements; F.D., G.B. and M.-C.A. performed the semiconductor heterostructure growth; M.A.B. conceived the concept and the experiment; M.A.B. and A.A. developed the concept and planned and directed the research; and J.L., M.T., C.A., A.A. and M.A.B. wrote the manuscript.

Author Information Reprints and permissions information is available at www.nature.com/reprints. The authors declare no competing financial interests. Readers are welcome to comment on the online version of the paper. Correspondence and requests for materials should be addressed to M.A.B. (mbelkin@ece.utexas.edu).

METHODS

Intersubband absorption measurements. Extended Data Fig. 1 shows the experimentally measured intersubband absorption spectrum after background correction. The spectrum is obtained in a multipass geometry using the original InP wafer with the MQW layer on top. The wafer was polished to have facets at 45° to the surface normal and its top and bottom surfaces were gold-coated, as shown in the inset to Extended Data Fig. 1. This measurement approach follows a standard procedure as described, for example, in ref. 3. Assuming unpolarized sample illumination from the Fourier Transform Infrared Spectrometer (FTIR) thermal source and neglecting standing wave effects, the intersubband absorption coefficient α_W is given as[3]:

$$\alpha_W = -\frac{1}{L_{\mathrm{int}}}\ln(10)\log_{10}\left(\frac{I_{\mathrm{TM}}}{I_{\mathrm{TE}}}\right) \tag{2}$$

where I_{TE} and I_{TM} are the transmitted intensities of TE- and TM-polarized light, respectively, and L_{int} is the interaction length defined as[3]

$$\mathrm{L}_{\mathrm{int}} = \frac{\mathrm{n_p} L_{\mathrm{QW}} N}{\cos(\theta)} \tag{3}$$

where θ is the angle of incidence with respect to the normal to the plane of the layers (45° in our case), L_{QW} is the thickness of each coupled quantum well section ($L_{\mathrm{QW}} = 20.6$ nm in our case), N is the total number of sections in the MQW sample ($N = 28$ in our case), and n_{p} is the number of passes through the MQW layer. Given our sample geometry (5 mm in length and 0.33 mm in thickness), we estimate $n_{\mathrm{p}} = 14$. From Extended Data Fig. 1, we obtain transition energies $\hbar\omega_{21} \approx 155$ meV and $\hbar\omega_{31} \approx 306$ meV in excellent agreement with calculated values of 153 meV and 306 meV, respectively, as shown in Fig. 1a. The measured transition linewidths are $2\hbar\gamma_{21} \approx 15$ meV, $2\hbar\gamma_{31} \approx 17$ meV and the peak absorption $\alpha_W = 615\ \mathrm{cm}^{-1}$ and $171\ \mathrm{cm}^{-1}$ for the 2–1 transition and the 3–1 transition, respectively. Given the close agreement between calculated and measured transition energies and the typically high accuracy of band-structure calculations, we assume that the transition dipole moments for intersubband transitions between states 1, 2 and 3 in our structure are the same as simulated in Fig. 1a. The values of intersubband absorption α_W then allows us to estimate the actual doping level N_e in our structure, which may be different from the nominal doping used during growth. To that end, we express α_W through the dielectric constant for out-of-plane ($\varepsilon_\perp$) E-field polarization as[3]

$$\alpha_W = 2\frac{\omega}{c}\mathrm{Im}(\sqrt{\varepsilon_\perp})\sin^2(\theta) \tag{4}$$

where

$$\varepsilon_\perp(\omega) \approx \varepsilon_{\mathrm{core}}(\omega) + \frac{N_e(ez_{12})^2}{\varepsilon_0\hbar((\omega_{21}-\omega)-i\gamma_{21})} + \frac{N_e(ez_{31})^2}{\varepsilon_0\hbar((\omega_{31}-\omega)-i\gamma_{31})} \tag{5}$$

where $\varepsilon_{\mathrm{core}}$ is the dielectric constant of the undoped heterostructures. Putting the experimental values of $\hbar\omega_{ij}$ and $\hbar\gamma_{ij}$, and calculated transition dipole moments z_{ij}, into the expressions above we obtain $\alpha_W \approx 620\ \mathrm{cm}^{-1}$ at the 2–1 resonance and $\alpha_W \approx 180\ \mathrm{cm}^{-1}$ at the 3–1 resonance using $N_e = 0.75 \times 10^{17}\ \mathrm{cm}^{-3}$, in close agreement with measurements. It is the value that is used for $\chi^{(2)}$ calculations. We note that the experimental value of N_e is a factor of 2 smaller than the nominal doping density.

Calculations of the optical properties of the MQW layer and plasmonic nanoresonators. The expression for the intersubband nonlinear susceptibility tensor element for SHG at pump frequencies close to intersubband resonances may be approximately written as[27]:

$$\chi^{(2)}_{zzz}(\omega\rightarrow 2\omega) \approx N_e\frac{e^3}{\hbar^2\varepsilon_0}\frac{z_{12}z_{23}z_{31}}{(\omega_{31}-2\omega-i\gamma_{31})(\omega_{21}-\omega-i\gamma_{21})} \tag{6}$$

where ω is the pump frequency, e is the electron charge, N_e is the average bulk doping density, $\hbar\omega_{ij}$, $\hbar\gamma_{ij}$ and ez_{ij} are the energy, linewidth and dipole moment, respectively, for a transition between states i and j. The values of $\chi^{(2)}_{zzz}$ in Fig. 1b are calculated using the expression above, assuming calculated transition dipole moments ez_{ij} and experimentally measured values of $\hbar\omega_{21} \approx 155$ meV, $\hbar\omega_{21} \approx 306$ meV, $2\hbar\gamma_{21} \approx 15$ meV, $2\hbar\gamma_{31} \approx 17$ meV and $N_e \approx 0.75 \times 10^{17}\ \mathrm{cm}^{-3}$ obtained from intersubband absorption measurements as described above.

The dielectric constant in the MQW layer for the out-of-plane ($\varepsilon_\perp$) E-field polarization is given in equation (5), the dielectric constant for the in-plane ($\varepsilon_{//}$) E-field polarization is calculated as

$$\varepsilon_{//}(\omega) \approx \varepsilon_{\mathrm{core}}(\omega) + i\frac{N_e e^2\tau}{\varepsilon_0\omega m^*(1-i\omega\tau_{\mathrm{D}})} \tag{7}$$

where $\varepsilon_{\mathrm{core}}(\omega)$ is the dielectric constant of the MQW with $N_e = 0$ and the electrons' motion in the plane of the semiconductor layers is assumed to be free with Drude relaxation time $\tau_{\mathrm{D}} \approx 10^{-13}$ s, which is a typical value for the InGaAs/AlInAs material with low doping density.

A commercial Maxwell's equations solver based on the finite-integration method was used to compute the E-field distribution in the MQW layer at different input frequencies. Periodic boundary conditions were placed around the unit cell, which included the plasmonic resonator made of a 50-nm-thick layer of gold, a 400-nm-thick MQW layer, a ground plane made of a 50-nm-thick layer of platinum (Pt) and a 100-nm-thick layer of gold. The transmittance of the metasurface was zero ($T = 0$) and the absorbance A was calculated as $A = 1 - R$, where R is the reflectance of both co-polar and cross-polar mode contributions.

Nonlinear optical response of the metasurface. The nonlinear response of the proposed metasurface, summarized by equation (1) in the main text, may be evaluated using the Lorentz reciprocity theorem, under the assumption that saturation effects can be neglected. Essentially, we relate the linear optical response of the metasurface at the fundamental (pump) and second harmonic frequencies to its nonlinear interaction: the Lorentz reciprocity theorem states that if the current density $\mathbf{J}_1$ at point $\mathbf{r}_1$ produces an electric field $\mathbf{E}_1$ at point $\mathbf{r}_2$, then by switching the position of source and observation, their product remains constant, that is:

$$\int_V J_1\cdot E_2\,\mathrm{d}V = \int_V E_1\cdot J_2\,\mathrm{d}V \tag{8}$$

In our case, the electric field $E_z^\omega(x,y,z)$ induced at the fundamental frequency in the MQW layer produces an equivalent current density distribution at the SH frequency given by:

$$J^{2\omega}(x,y,z) = j2\omega P^{2\omega}(x,y,z) = j2\omega\varepsilon_0\chi^{(2)}E_z^\omega(x,y,z)^2 \tag{9}$$

We can now apply reciprocity considerations at the SH frequency to relate the field distribution $E_z^{2\omega}(x,y,z)$, induced in the metasurface volume by a plane wave impinging at normal incidence, to the radiated field $E_{\mathrm{FF}}^{2\omega}$ sustained by the currents $J^{2\omega}(x,y,z)$. The formula yields:

$$\int_{V_{\mathrm{MQW}}} J^{2\omega}(x,y,z)E_z^{2\omega}(x,y,z)\,\mathrm{d}V = \int_{V_{\mathrm{FF}}} E_{\mathrm{FF}}^{2\omega}J_{\mathrm{FF}}^{2\omega}\,\mathrm{d}V \tag{10}$$

where $J_{\mathrm{FF}}^{2\omega}$ is the current density necessary to sustain the impinging plane wave inducing $E_z^{2\omega}(x,y,z)$ placed in the volume V_{FF}, and V_{MQW} is the volume of the MQW substrate. After simple algebraic manipulations, one can relate the radiated fields to the field distributions in the MQW layer at FF and SH frequencies:

$$E_{\mathrm{FF}}^{2\omega} = \frac{j\omega\chi^{(2)}}{c_0 E_{\mathrm{inc}}^{2\omega}S_{\mathrm{unit}}}\int_{V_{\mathrm{unit}}} E_z^\omega(x,y,z)^2 E_z^{2\omega}(x,y,z)\,\mathrm{d}V \tag{11}$$

where S_{unit} is the surface area of the unit cell of the periodic metasurface and V_{unit} is the volume of the MQW within the same unit cell. Generalizing this formalism to the arbitrary polarization of impinging and radiated fields, we obtain equation (1) in the main text for each element of the effective nonlinear tensor $\chi_{ijk}^{(2)\mathrm{eff}}$. The SHG conversion efficiency is then calculated from the ratio of the radiated second-harmonic power over the impinging power:

$$\mathrm{SHG_{eff}} = \left|\frac{j\omega\chi^{(2)}}{c_0 E_{\mathrm{inc}}^{2\omega}E_{\mathrm{inc}}^{\omega}S_{\mathrm{unit}}}\int_{V_{\mathrm{unit}}} E_z^\omega(x,y,z)^2 E_z^{2\omega}(x,y,z)\,\mathrm{d}V\right|^2 \tag{12}$$

In the special case in which we can assume that the field distributions are constant inside the MQW layer at both FF and SH frequencies, the SHG efficiency simply becomes $\mathrm{SHG_{eff}} = \frac{1}{2}\omega^2\eta_0^3\left|\varepsilon_0\chi^{(2)}_{zzz}\right|^2 f_{2\omega}^2 f_\omega^4 I_\omega L^2$, where η_0 is the impedance of free space, f_ω the field enhancement factor at the FF, $f_{2\omega}$ is the field enhancement at the SH, I_ω is the input intensity and L is the height of the MQW layer, as expected.

From equation (12) we can obtain the expression for SHG intensity output $I_{2\omega}$ from the metasurface

$$I_{2\omega} = \frac{(2\omega)^2}{8\varepsilon_0 c^3}\left|\hat{e}_{2\omega}\overset{\leftrightarrow}{\chi}^{(2)\mathrm{eff}}\hat{e}_\omega\hat{e}_\omega\right|^2(I_\omega)^2 L^2 \tag{13}$$

where $\hat{e}_{2\omega}(\hat{e}_\omega)$ and $I_{2\omega}$ (I_ω) are the polarization unit vector and intensity, respectively, of the SH (FF) beams, L is the MQW thickness and $\overset{\leftrightarrow}{\chi}^{(2)\mathrm{eff}}$ is given by equation (1) which includes local field enhancement at both ω and 2ω. We note that this expression is consistent with the conventional formula to express the SHG in regular nonlinear crystals, assuming that the thickness L is much smaller than the coherence length[27].

Fabrication. The nonlinear MQW structure used in our experiments was initially made of 28 repetitions of the $\mathrm{In_{0.53}Ga_{0.47}As/Al_{0.48}In_{0.52}As}$ coupled-quantum well structure shown in Fig. 1a for a total thickness of 577 nm. It was then thinned down to approximately 400 nm thickness by chemical etching. The layer sequence (in nanometres) is **6.0**/5.3/**1**/2.3/**6.0** where AlInAs barriers are shown in bold. The first 3 nm of a first 6-nm barrier and the last 3 nm of the last 6-nm barrier are n-doped to 5×10^{17} cm^{-3}. The structure was grown by molecular beam epitaxy on a semi-insulating InP substrate. The growth started with a 300-nm-thick etch-stop layer of $\mathrm{In_{0.53}Ga_{0.47}As}$, followed by a 100-nm-thick etch-stop layer of InP, followed by the MQW layer. A 10-nm-thick layer of titanium, a 50-nm-thick layer of platinum, and a 500-nm-thick layer of gold were then sequentially evaporated on top of the MQW layer. The wafer was then thermo-compressively bonded epi-side down to a semi-insulating InP wafer coated with same metal layers. The substrate was removed via selective chemical wet-etching, followed by the removal of the etch-stop layers via selective wet-etching to expose the MQW layer. Plasmonic nanostructures were defined on the MQW layer via e-beam lithography and evaporation of a 5-nm-thick layer of titanium and 50-nm-thick layer of gold, followed by lift-off.

Optical measurements. Linear optical characterization of the metasurface was done in reflection mode using a FTIR spectrometer equipped with a liquid nitrogen cooled HgCdTe photo-detector. Nonlinear properties of the metasurface were probed by a pulsed broadly-tunable quantum cascade laser (Daylight Solutions; tuning range 1,120–1,450 cm^{-1} and peak power output 800 mW). The laser was operated with 400-ns-long pulses at 250 kHz repetition frequency. Details of the optical set-up are shown in Fig. 3d. We assume a Gaussian beam shape on the metasurface with an intensity distribution for FF given as $I_{\mathrm{FF}} e^{-2r^2/w^2}$ and that for SH frequency as $I_{\mathrm{SH}} e^{-4r^2/w^2}$. The FF focal spot diameter was measured by the knife-edge technique to be $2w = 35$ μm. A calibrated InSb detector was used to measure SHG power output and perform spectroscopic measurements at SHG frequencies. SHG power output was corrected for the beam splitter reflectivity (47.5%) and the transmission of the collimating lens (95%), the polarizer (82%), the ZnSe lens (97%), and the shortpass filter (83.5%) in the set-up. A calibrated thermopile detector was used to determine the power of the fundamental beam at the sample position. The values of $\overset{\leftrightarrow}{\chi}^{(2)\mathrm{eff}}$ tensor elements were deduced using the $I_{2\omega}$ expression presented in the 'Calculations' section, based on the experimentally measured values of $I_{2\omega}$ and I_{ω}.

Structures with plasmonic resonances detuned from intersubband transition frequencies. Over the course of our experimental work, we have fabricated a number of metasurfaces in which plasmonic resonances happened to occur away from the intersubband $\left|\chi_{zzz}^{(2)}\right|$ peak, and those structures produced little or no detectable SHG response. An example of such a metasurface is shown in Extended Data Fig. 2. These measurements confirm that the giant nonlinear effects observed in our optimized structures stem from the combination of quantum engineering of the nonlinear response coming from the MQW intersubband transition and the electromagnetic resonance engineering of the coupled metasurface.

Nonlinear response saturation mechanism. Saturation intensity for our MQW structure can be estimated with the expression from ref. 33

$$I_{\mathrm{sat}} = \frac{cn\varepsilon_0\hbar^2}{e^2 z_{12}^2 \tau g(\nu)} \qquad (14)$$

where $n \approx 3.2$ is the refractive index of MQW, τ is the state 2 lifetime computed to be 1.7 ps and $g(\nu)$ is the normalized Lorentzian lineshape function, $g(\nu) = 2\hbar \dfrac{\gamma_{21}}{(h\nu - E_{21})^2 + \gamma_{21}^2}$. Substituting measured $2\hbar\gamma_{21} \approx 15$ meV and computed $z_{12} = 1.7$ nm into equation (14) we obtain $I_{\mathrm{sat}} = 0.47$ MW cm^{-2} for resonant excitation of the 1–2 transition.

To confirm that the observed saturation of SHG conversion efficiency is not due to thermal effects, SHG measurements were repeated using 60-ns light pulses. Extended Data Fig. 3a compares the results of these measurements with those obtained using 400-ns current pulses as reported in the main text and shows that results are in nearly perfect agreement, which excludes thermal effects in the observed SHG response.

If we detune the pump frequency, moving away from the design frequency at which intersubband absorption and plasmonic metasurface resonance take place, and therefore reducing the field intensity in the multi-quantum well substrate, the saturation is significantly reduced, as shown in Extended Data Fig. 3b.

SHG generation at oblique incidence. The nonlinear metasurface described in the main text can also operate as an SHG mirror at oblique incidence angles. This is because enhanced wave–matter interaction arises at the short scale, supported by the inclusion resonances, rather than based on a collective effect. Extended Data Fig. 4a and b shows details of SHG power output measurements at 45° angle of incidence pumping. Nonlinear response that was comparable to that reported for normal incidence in Fig. 4a was observed for SSS, PPP, SPP and PSS polarization combinations, as shown in Extended Data Fig. 4b. In our notation, the first of three letters in the polarization combination refers to the polarization of the SHG wave and the last two letters refer to the polarization of the input fundamental frequency with E-field directions for S and P polarizations shown in Extended Data Fig. 4a.

For a control experiment, we used a bare MQW structure without plasmonic nanostructures, which produced no detectable SHG response in this configuration for all polarization combinations. We note that in principle one expects to have some nonlinear response for the PPP polarization combination from bare MQW structures in this experimental configuration due to the presence of intersubband $\chi_{zzz}^{(2)}$. However, due to the insufficient thickness of the sample and the small value of E_z field inside the MQW material this 'intrinsic' intersubband response was below our detection limit.

Extended Data Fig. 4c shows the simulated absorption of our metasurface at 45° incidence for S and P light polarizations. We note that the absorption peak positions are not significantly affected by the change in excitation angle, due to the local response of the metasurface inclusions. It is therefore appropriate to use the nonlinear mirror in reflection mode without constraints on the incidence and observation angle.

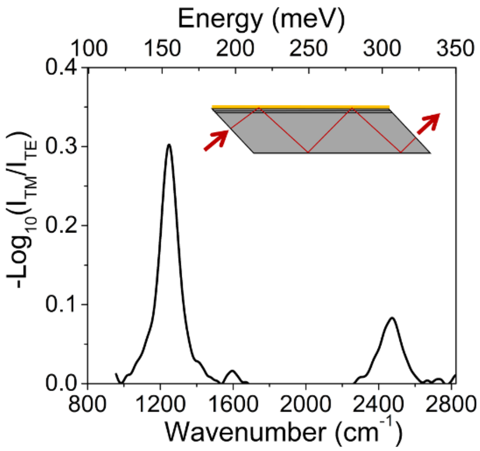

Extended Data Figure 1 | Intersubband absorption measurement. Intersubband absorption spectrum of the wafer used in our experiments after background correction. Bottom *y* axis, wavenumber (=1/λ); top *y* axis, energy (=$h\nu$). Inset, measurement geometry.

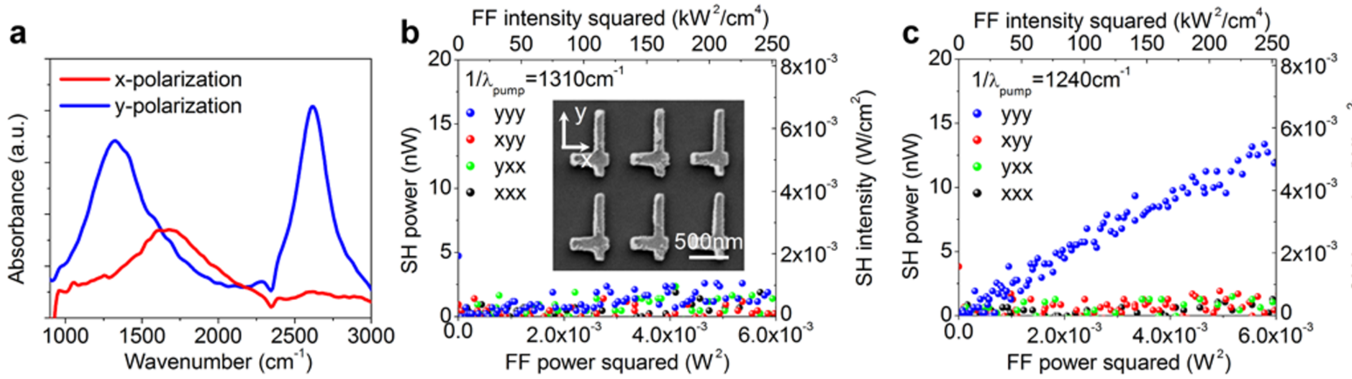

Extended Data Figure 2 | Structures with plasmonic resonances detuned from intersubband transition frequencies. **a**, Linear absorption spectrum of a metasurface in which plasmonic resonances were not well-overlapped spectrally with intersubband transitions of the MQW structure for fundamental and SH frequencies. **b**, SH peak power (left axis) or intensity (right axis) as a function of FF peak power squared (bottom axis) or peak intensity squared (top axis) for different input/output polarization combinations (*yyy* and so on, see key) at FF pump wavenumber $1/\lambda_{\mathrm{pump}} = 1{,}310\,\mathrm{cm}^{-1}$ and SH wavenumber $2{,}620\,\mathrm{cm}^{-1}$ both in resonance with the plasmonic absorption peaks. SH response was close to the noise limit of our setup. Inset, SEM image of the metasurface. **c**, SH peak power output as a function of FF peak power squared (bottom axis) or peak intensity squared (top axis) for different input/output polarization combinations at FF wavenumber $1{,}240\,\mathrm{cm}^{-1}$ and SHG wavenumber of $2{,}480\,\mathrm{cm}^{-1}$, both away from plasmonic resonances of the metasurface but in resonance with intersubband transitions in the MQW structure.

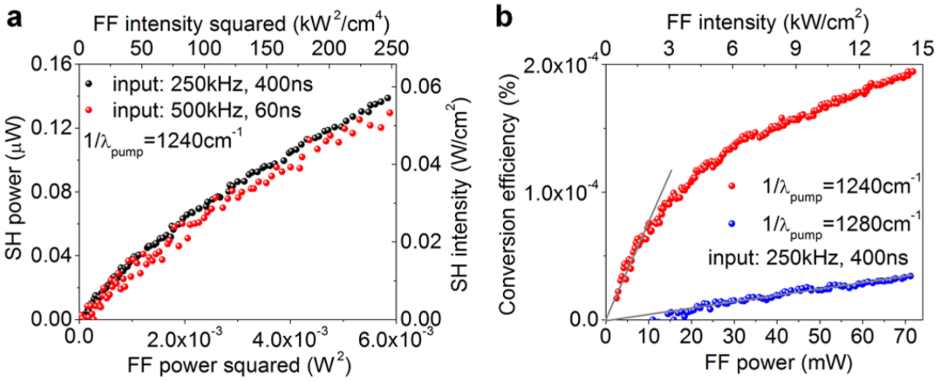

Extended Data Figure 3 | Nonlinear response saturation mechanism. **a**, SH peak power output as a function of FF peak power squared (bottom axis) or peak intensity squared (top axis) at FF wavenumber 1,240 cm^{-1}. Black curve, data for the pump laser operating with 400 ns pulses (same as used in the main text); red curve, data for the pump laser operating with 60 ns pulses. A slight difference in the SHG power for 60 ns and 400 ns FF input is attributed to slight changes in the pulse shape and detector response for 400 ns and 60 ns pulses. **b**, SH conversion efficiency versus FF peak power (bottom axis) or peak intensity (top axis) for FF wavenumber 1,240 cm^{-1} (red) and 1,280 cm^{-1} (blue). Straight lines show expected linear dependence of SH conversion efficiency on FF power for the cases in the absence of intensity saturation.

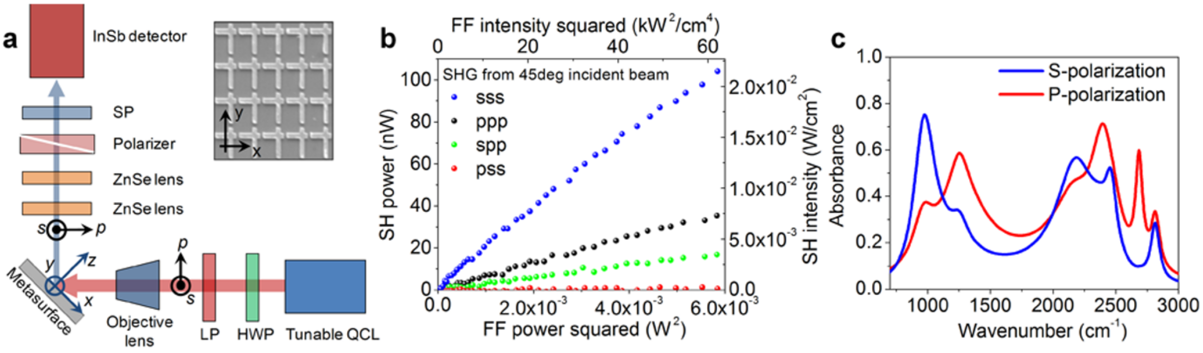

Extended Data Figure 4 | SHG at oblique incidence. **a**, Optical set-up for metasurface characterization at 45° incidence angle. LP and SP are long- and short-pulse filters, respectively. HWP is a half-wave plate for FF polarization control. Directions of S- and P-polarizations and orientation of the metasurface are indicated. Inset, SEM image of the metasurface with *x* and *y* axes shown. **b**, Measured SH peak power output as a function of FF peak power squared (bottom axis) or peak intensity squared (top axis) at FF wavenumber 1,240 cm^{-1} for different input/output polarization combinations (SSS and so on, see key). **c**, Simulated absorption spectrum of the metasurface at 45° incidence for different input light polarizations.